Bulletin of the Seismological Society of America, Vol. 92, No. 4, pp. 1208–1226, May 2002

Source Description of the 1999 Hector Mine, California, Earthquake, Part II: Complexity of Slip History

by Chen Ji, David J. Wald, and Donald V. Helmberger

Abstract We present a rupture model of the Hector Mine earthquake (*M* 7.1), determined from the joint inversion of strong-motion records, *P* and *SH* teleseismic body waves, Global Positioning System (GPS) displacement vectors, and measured surface offset. We solve for variable local slip, rake angle, rise time, and rupture velocity of a finite-fault model involving multiple segments. The inversion methodology developed in a companion article (Ji *et al.*, 2002) combines a wavelet transform approach with a nonlinear (simulated annealing) algorithm. The final model is checked by forward simulating the Interferometric Synthetic Aperture Radar (InSar) data. Our estimation to the seismic moment is 6.28×10^{19} N m, which is distributed along three segments from north to south, releasing 37%, 41%, and 22% of the total moment, respectively. The average slip is 1.5 m, with peak amplitudes as high as 7 m. The fault rupture has an average rise time of 3.5 sec and a relatively slow average rupture velocity (1.9 km/sec) resulting in a 14-sec rupture propagation history. Our approach permits large variation in rupture velocity and rise time, and indicates that rise time appears to be roughly proportional to slip and shorter rise times are associated with the initiation of asperity rupture. We also find evidence for nearly simultaneous rupture of the two northern branches.

Introduction

The M_w 7.1 Hector Mine, California, earthquake occurred in a remote, sparsely populated part of the Mojave desert, only about 20 km east of the 1992 M_w 7.3 Landers earthquake. Both occurred within the eastern California shear zone (ECSZ). Because most of faults in the ECSZ have low slip rates and major earthquake repeat times are on the order of several thousands to tens of thousands of years (Sieh *et al.*, 1993), the occurrence of two $M_w > 7$ earthquakes within 7 years illustrates the complexity of the faulting interaction.

The Hector Mine earthquake occurred when major upgrades to the regional seismic network (TriNet) were underway (Mori *et al.*, 1999). With the convenient real-time TriNet data set, the basic source information of this earthquake was obtained soon after it occurred. For instance, the focal mechanism was determined within a minute (Zhu and Helmberger, 1996). After a few hours, even a preliminary single-plane finite-fault model was determined using waveform data from the TriNet array (Dreger and Kaverina, 2000).

As the accumulation of information continued, however, discrepancies became apparent. One discrepancy is the difference between the surface rupture (Fig. 1) and the preliminary finite-fault model. Most of the surface break (more than 5 m at some sites) was centered around the hypocenter, but is nearly zero in the preliminary finite-fault model (Dreger and Kaverina, 2000). In contrast, in the 1992 Landers earthquake, the initial models constrained by the seismic data were consistent with the geological observations (e.g., Kanamori *et al.*, 1992; Dreger, 1994).

Dreger and Kaverina (2000) approximated the complex fault geometry of the Hector Mine earthquake by a single plane, because the goal was to obtain a finite-fault model in near real time. Here, we want to show that the discrepancies can be explained by considering the fault geometry and rupture initiation. The surface break data and aftershock pattern are, in fact, used to determine the complexity of the fault plane geometry. The local strong-motion data, teleseismic body waves, and GPS data are combined to constrain the slip history of the Hector Mine earthquake.

One of the unique advantages of the strong-motion records of this event is the timing. Traditionally, strong-motion instruments were designed for engineering purposes and thus they did not record continuously. They were triggered when ground accelerations were larger than a particular threshold, and the absolute trigger time was often not preserved. Usually, it is assumed that the instruments are triggered by the direct *P* waves (e.g., Hartzell and Heaton, 1983). This assumption may not be valid, because most large earthquakes start with a foreshock or nucleation phase (Ellsworth and Beroza, 1995). However, most of the strong mo-

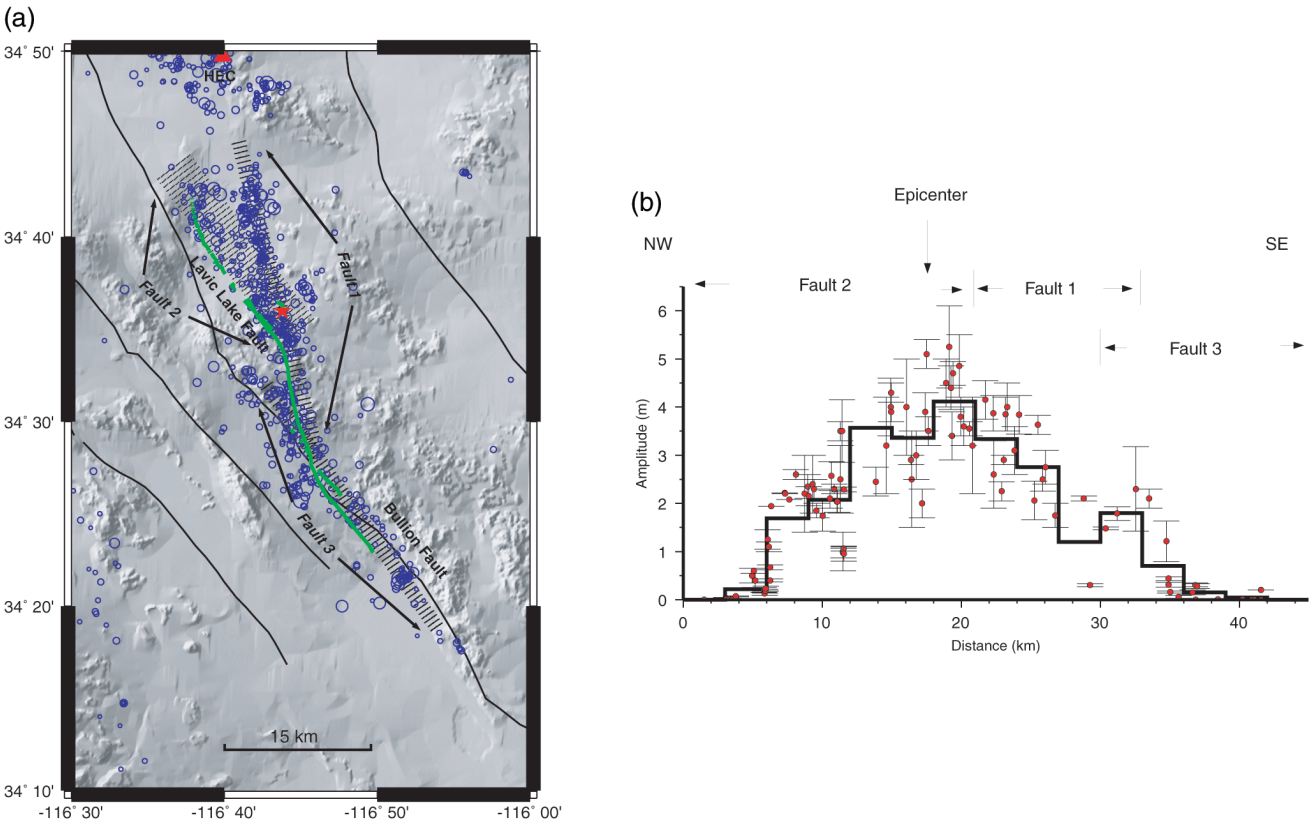

Figure 1. (a) Fault geometry for the 1999 Hector Mine earthquake, with a base map of local topography. The thin lines show major faults. The green traces indicate the mapped surface ruptures, the southern portion is associated with the Bullion fault, and the northern portion is the Lavic Lake fault. The star indicates the epicenter. Aftershocks ($M_L > 2$, Hauksson *et al.*, 2002) are plotted as blue circles. The grid of black dots is the surface projection of the point sources used to generate the fault response. The red triangle in the north is the location of TriNet station HEC. (b) Horizontal component of the slip on the surface rupture of the Hector Mine event. The red dots with error bars are surface measurements (Scientists of the USGS et al., 2000). The heavy line segments indicate the amount of the slip as averaged along 3-km intervals.

tions of the Hector Mine earthquake were recorded continuously at the broadband TriNet stations. Careful analysis of the beginning portions of the broadband records in absolute time was essential for determining the nucleation and evolution of this earthquake.

While the constraint to the slip distribution can be improved by additional geodetic data (Graves and Wald, 2001; Wald and Graves, 2001), the resolution of rupture evolution is still dependent on the wavelength of radiated seismic waves. Generally, the shorter the wavelength is, the higher the potential resolution is (Aki and Richards, 1980). In our companion article (Ji *et al.*, 2002), we incorporated the wavelet transform into a finite-fault inversion. The seismic data are further separated into multiple wavelet channels with different frequency bands. The lower-frequency channels are used to constrain the larger-scale characteristics of faults, and high-frequency channels help to constrain the pattern recognition. We apply this approach here to recover simultaneously the spatial variations of the slip amplitude, rake angle, rise time, and rupture time.

Preliminary Observations and Fault Geometry

The Hector Mine earthquake ruptured two fault zones, the Bullion fault and the Lavic Lake fault. The latter was mapped only after this earthquake (Fig. 1). The overall length of surface faulting is approximately 41 km, but most of the surface slip is along the central part of Lavic Lake fault, where the surface rupture changes direction. The strike changes from 322° in the north segment to 346° in the south. The maximum amplitude of surface slip (5.2 m) was measured near the intersection of the two surface breaks (Scientists of the USGS *et al.*, 2000). Surface slip along the Bullion fault (southern branch) is complex and smaller than along the Lavic Lake fault.

It is noteworthy that the surface slip in the northern portion shows two branches. In addition to the aforementioned larger surface break in the west, there is a small patch of surface rupture positioned directly above the hypocenter and along the northward extension of the middle portion (Fig. 1a). This implies that the Lavic Lake fault separates

into two faults. This observation is supported by the aftershock pattern, which shows two planes in the northern part of the Lavic Lake fault (Hauksson *et al.*, 2002). One plane has an azimuth of 322° trace and a dip angle of 75°. The other plane strikes 346° and is slightly steeper (85° to the east). While the former plane corresponds to the larger surface break, the hypocenter determined by local short period data is on the latter fault plane. The two-fault system can also explain the large variations in point source solutions obtained by several groups (Table 1). Even though all of the solutions indicated that the Hector Mine event is a nearly pure strike-slip earthquake, the strike directions vary between 329° and 343°, roughly in the middle of two fault planes determined by the aftershock pattern. We show later that the 20° difference in fault direction strongly affects the waveforms at the closest station, HEC.

Fault Parameterization

Based on the information just noted, we separate the rupture into three segments (Fig. 1). Fault 1 is the central part of the fault system, with a strike of 346° and a dip of 85°. Fault 2 is the northwestern segment, with a strike of 322° and a dip of 75°. Fault 3 is the southeastern segment, with a strike of 322° and a dip of 75°. We let fault 1 extend north of its junction with fault 2, and fault 3 extend north of its junction with fault 1, to guarantee the full coverage of the possible slip regions.

Here, the maximum depth of fault planes is fixed to be 16 km, because preliminary inversions with the bottom at 25 km did not show important deeper slip (>1 m). We use the epicenter from TriNet (34.597° N, −116.27° E) and let the main rupture nucleate in fault 1. The three fault segments are further divided into 168 subfaults with dimensions of 3 by 2.7 km. Four parameters (dislocation amplitude, rake angle, rise time, and rupture velocity) are used to control the response of each subfault (Ji *et al.*, 2002). Thus, we have 704 variables to solve in the inversions.

The Mojave velocity model (Fig. 2) (Jones and Helmberger, 1998) is in very good agreement with the average East Mojave model in the recently developed 3D tomography model of Hauksson (2000). It was also found to work well in explaining the waveforms for Landers aftershock sequence (Jones and Helmberger, 1998). Because of the similar station event paths for the Landers aftershocks and the Hector Mine earthquake, we chose this model to calculate the subfault Green's functions (Ji *et al.*, 2002).

The simulated annealing method (Sen and Stoffa, 1991) is applied to find a global minimum of the error function represented as

$$\mathrm{err}_{\mathrm{wf}} + W_{\mathrm{st}} \cdot \mathrm{err}_{\mathrm{st}} + W_{\mathrm{c}} \,(\mathrm{constraints}) = \mathrm{minimum} \quad (1)$$

Here, $\mathrm{err}_{\mathrm{wf}}$ and $\mathrm{err}_{\mathrm{st}}$ are objective functions of the seismic waveforms and static displacements, respectively. Two types of constraints are chosen: one that minimizes the difference in slip on adjacent subfaults and a second that minimizes the total moment (Hartzell *et al.*, 1996). The W_{st} and W_{c} are weights to the static criteria and constraints. Note that the objective functions and constraints have been normalized for the convenience of discussion (Ji *et al.*, 2002).

Table 1
Focal Mechanisms of the 1999 Hector Mine Earthquake

Groups	θ(°)	δ(°)	λ(°)	$M_o(10^{19}$ Nm)
Harvard	336	80	174	5.98
NEIC	329	83	171	5.4
TriNet	331	77	179	3.4
USB	343	70	175	4.01

θ, δ, and λ are the strike, dip and rake of the double couple fault plane which is close to the strike of the fault surface break, respectively.

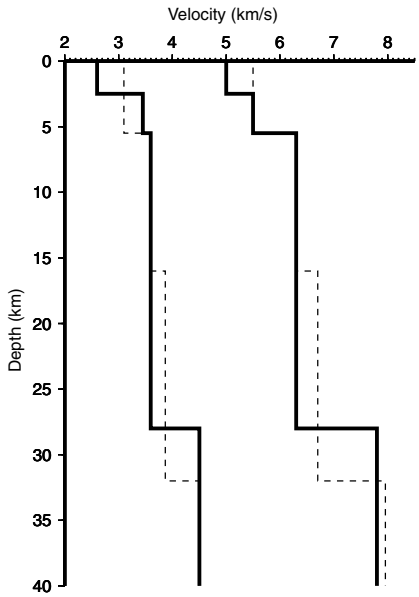

Figure 2. Layered velocity models. The solid lines show the Mojave model (Jones and Helmberger, 1998) and the dashed lines show the Southern California standard model (SoCal; Dreger and Helmberger, 1993).

After performing the test runs with larger ranges but rough intervals, the inversions presented here are constrained in the following ranges: the dislocation amplitude of each subfault is allowed to vary from 0 to 800 cm, and the rake angle can vary from 140° to 210°. The average rupture velocity is selected to range from 1.6 to 3.0 km/sec at intervals of 0.1 km/sec. Finally, the rise time is allowed to change from 0.6 to 6 sec at 0.6-sec intervals.

Data Sets

In this study, both seismic waveform data and geodetic data are used to constrain the fault model. The combination can offer a more uniform near-source coverage of the faults

and a more broadband frequency range of information (DC to 0.8 Hz) than the individual data sets.

Waveform Data

We use strong-motion data from 10 TriNet stations (table 2 and Fig. 3). These observations provide good azimuthal coverage, but only one station is less than 30 km from the epicenter of the mainshock, and most epicentral distances are between 75 km to 100 km. The lack of near-source stations limits the inverse resolution and robustness to the accuracy of the velocity structures used.

Most of the data were recorded on the broadband acceleration channels of TriNet stations. We deconvolve the instrument responses to obtain the ground velocities. However, the E–W component of record at station HEC was contaminated by the possible station tilt and by an aftershock that occurred about 60 sec after the mainshock. These data were corrected by removing a linear trend. The data of stations WWC, JTF, and FLS were high-pass filtered at 0.02 Hz to remove the uncertainty at the lower frequency, then integrated to velocities. All data are filtered by a fourth-order, two-pass butterworth filter to less than 1 Hz, then resampled to a sample interval of 0.2 sec.

All strong-motion data are aligned by the first arrivals of *P* waves. For continuous recording instruments, including all TriNet broadband stations, it was easy to identity the first arrivals. For the records in the triggered strong-motion stations WWC and JTF, the exact first-arrival times are not available, so we use the Mojave velocity model to estimate them. Such values are adjusted by performing a preliminary inversion based on weighting only the other stations and then comparing the synthetic and observed waveforms at triggered stations. The times are not changed during the subsequent inversions.

Note that we did not rotate the records to fault normal and parallel, because the extended fault length makes rotation ambiguous. The horizontal components were given twice the weight of those for the vertical components because the vertical components are dominated by *P* waves, which are not as well modeled by our simple 1D velocity model. During the inversion, both data and synthetic were normalized with the peak amplitude of data to avoid any bias by the larger-amplitude stations. Moreover, we gave the closest station HEC the largest weight (Table 2), because such close-fault records have larger sensitivity to the slip model than more distant data.

Fifteen teleseismic *P* waves and 11 *SH* waves are also used in our inversions. These data provide a well-distributed azimuth coverage of the source (Table 3). The instrument responses were deconvolved from the original records to obtain ground velocities. Finally, the data were also low-pass filtered to less than 1 Hz by a fourth-order two-pass butterworth filter, and resampled to a sample interval of 0.2 sec to be compatible with the strong-motion data.

Because of the existence of a small foreshock (Appendix A), the teleseismic arrival times are very difficult to pick.

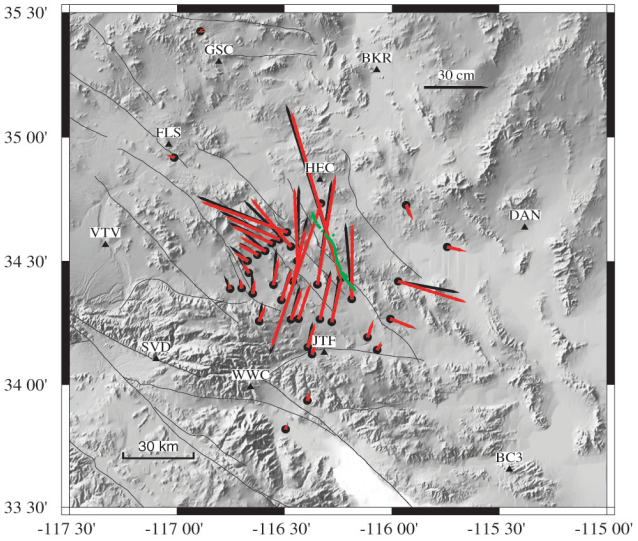

Figure 3. Distribution of strong-motion stations (triangles) and GPS stations (circles). Thick lines show the surface rupture of the Hector Mine earthquake. Comparison of the horizontal GPS data (black arrows) and synthetic static displacements (red arrows) generated by the preferred model is also shown.

We use the Iasp91 travel-time table (Kennett and Engdahl, 1991) to make first-order estimations. However, these estimations alone are not sufficient to be used directly in a waveform inversion. For instance, in their study of 1992 Landers earthquake, Wald and Heaton (1994) found that the uncertainty in *P*-wave arrival time could greater than 2.0 sec. Considering the small spatial separation between two earthquakes, we believe that there is about the same amount of uncertainty in the current data set. Because of the small takeoff angles of the teleseismic phases, such uncertainty in the arrival-time estimations can cause important errors in inverted models; e.g., 1.0-sec error in teleseismic *P* arrival time implies greater than 10-km horizontal mislocation of the corresponding seismic radiation source. For this reason, we first use the strong-motion data to obtain a preliminary fault model, then apply the model to predict the teleseismic synthetic seismograms. Improved best alignments are estimated by comparing the synthetic and observed waveforms. Unfortunately, this procedure reduces the independence of teleseismic data to some extent.

During the inversions, the number of wavelet coefficients used depends on the quality of the Green's functions (Ji *et al.*, 2002). We use the wavelet coefficients with scales not smaller than 1.6 sec for most of the strong-motion and teleseismic *P* data, which is similar to a low-pass filter with a corner frequency at 0.6 Hz (Ji *et al.*, 2002). For the records of the closest station HEC, we put the coefficients with a scale of 0.8 sec into inversions. In contrast, for the *S* wave data, the high frequency cutoff is only 0.3 Hz (the scale $s \geq 3.2$ sec) because the 4.0-sec attenuation factor removes most higher-frequency energy.

Table 2
Strong-Motion Data

Sta	Lat (°)	Long (°)	Dist (km)	Az (°)	Affi	*W*(U–D)	*W*(N–S)	*W*(E–W)
HEC	34.829	−116.335	26.24	345.92	TriNet	1.5	4.0	4.0
BKR	35.269	−116.070	76.45	13.38	TriNet	1.0	1.5	1.5
DAN	34.637	−115.381	80.96	86.84	TriNet	0.5	1.0	1.0
GSC	35.302	−116.805	92.23	327.92	TriNet	0.5	1.0	1.0
SVD	34.104	−117.097	94.17	234.40	TriNet	1.0	1.5	1.5
VTV	34.567	−117.333	97.79	268.15	TriNet	1.0	1.5	1.5
BC3	33.655	−115.453	128.89	144.35	TriNet	0.5	1.0	1.0
JTF	34.130	−116.314	52.43	184.93	CDMG	1.0	1.5	1.5
WWC	33.990	−116.657	76.76	208.07	USGS	0.5	1.0	1.0
FLS	34.970	−117.039	81.75	300.42	USGS	0.5	1.0	1.0

Table 3
Teleseismic Data

Stations	Lat (°)	Long (°)	Dist (km)	Az (°)	*P*-delay(s)	*S*-delays(s)
ARU	56.43	58.56	89.18	2.84	0.6	—
ALE	82.50	−62.35	51.32	7.81	—	−3.2
RES	74.69	−94.90	41.55	8.40	0.6	—
KBS	78.93	11.94	62.89	9.81	0.4	—
OBN	55.11	36.57	87.63	15.19	0.0	—
KONO	59.65	9.60	76.03	25.06	0.0	—
SFJ	67.00	−50.62	49.16	28.23	—	0.0
BORG	64.75	−21.33	61.24	29.15	—	2.8
ESK	55.32	−3.21	73.82	33.18	0.4	—
MTE	40.40	−7.54	80.67	47.11	−0.2	—
SJG	18.11	−66.15	47.38	96.89	−0.6	0.2
NNA	−11.99	−76.84	59.55	133.79	−0.8	1.2
PAYG	−0.67	−90.29	42.68	139.64	0.0	—
RPN	−27.13	−109.33	61.78	172.98	—	3.4
MSVF	−17.73	178.05	81.28	241.50	—	5.4
KIP	21.42	−158.01	38.81	261.53	−1.8	—
ADK	51.88	−176.68	45.90	311.42	−2.2	−3.2
MA2	59.58	150.77	62.24	324.97	—	1.8
YAK	62.03	129.68	70.11	332.76	−2.8	—
COLA	64.87	−147.85	35.83	337.60	0.8	—
BILL	68.06	166.45	53.64	332.95	—	1.2
TIXI	71.65	128.87	64.69	341.48	—	−2.4
INK	68.31	−133.52	35.21	349.01	0.6	—

Geological and Geodetic Data

The field observations of the Hector Mine earthquake were made during the week following the mainshock (Scientists, of the USGS *et al.*, 2000). Since there is no evidence of large afterslip, it is a good data set to help constrain the fault model. The slip measurements along the surface rupture were made at evenly distributed points along the fault. For our finite-fault model, we average the detailed measured slip on 3- by 2.7-km subfaults because the distant and lower-pass filtered seismic data do not have enough resolution to distinguish smaller spatial heterogeneities. Following work of Wald and Heaton (1994), we average the measured surface slip within the 3-km intervals along surface subfaults (Fig. 1b). This averaging reduced the peak amplitude from 5.2 to 4.1 m.

The GPS data (Table 4) is another important dataset for our study. We use the horizontal and vertical displacements at 36 monuments of the Southern California Integrated GPS Network (SCIGN) and the U.S. Geological Survey (USGS) (Agnew *et al.*, 2002). Only stations with greater than 3 cm of horizontal displacement are chosen, to guarantee a good signal noise ratio. Since many of the GPS stations were operated to study the postseismic motion of the Landers earthquake, the coverage on the western side of the Lavic Lake fault is better than that on the eastern side (Fig. 3).

Finite-Fault Modeling

The slip distribution determined with the GPS data should be similar to that constrained by the seismic data,

Table 4
Comparison of Observed and Synthetic GPS Displacements

	Position °		U–D (cm)		N–S (cm)		E–W (cm)	
Site	Long	Lat	Obs	Syn	Obs	Syn	Obs	Syn
LAE1	−116.557	34.574	−7.10	−2.17	10.40	8.38	−20.80	−18.85
LAE2	−116.522	34.589	−1.30	−2.43	13.90	11.30	−28.00	−25.33
LAE3	−116.487	34.618	0.50	−2.00	17.70	15.08	−42.40	−40.29
LAE4	−116.329	34.734	−19.30	−16.81	−74.50	−70.83	−24.20	−23.26
LAW1	−116.588	34.542	−2.30	−1.67	11.60	7.03	−12.50	−11.92
LAW2	−116.624	34.527	−0.20	−1.35	6.10	5.41	−8.60	−9.24
LAW3	−116.669	34.502	0.40	−0.99	7.40	4.10	−8.60	−6.39
LAW4	−116.665	34.454	0.10	−0.53	8.30	4.95	−5.40	−3.07
MEEK	−116.617	34.258	0.10	0.80	9.70	7.58	1.40	2.96
OLDD	−116.698	34.391	−0.60	−0.08	4.70	4.58	−1.40	−0.54
OLDW	−116.752	34.389	−0.90	−0.15	6.70	3.25	−3.00	−1.05
RICH	−116.469	34.264	7.26	1.44	17.20	14.93	4.18	5.06
SANH	−116.279	34.255	1.05	1.94	23.07	21.92	3.66	4.62
CTMS	−116.370	34.124	1.40	1.44	10.50	10.23	3.13	2.78
LDES	−116.433	34.267	1.70	1.60	17.96	17.29	5.73	5.42
OAES	−116.068	34.141	0.21	0.50	2.80	4.09	2.48	2.00
WIDC	−116.392	33.935	0.33	0.87	5.26	4.68	1.57	1.22
BSRY	−117.012	34.919	−1.00	−0.77	1.53	1.38	−3.57	−3.57
PSAP	−116.494	33.819	0.71	0.68	3.15	3.07	1.11	0.19
AMBO	−115.742	34.559	−2.50	−1.10	−1.60	−2.13	7.00	8.51
0808	−115.933	34.728	2.60	0.21	−5.40	−7.25	1.30	3.02
SCP2	−115.969	34.419	−0.90	−1.47	−5.50	−10.22	28.40	31.66
SCP1	−116.006	34.267	−1.30	−0.41	−4.80	−4.72	12.00	11.40
MESQ	−116.113	34.193	0.20	0.84	6.90	8.09	2.30	2.60
SCP4	−116.186	34.348	−2.40	−0.29	37.60	36.56	−3.10	0.15
SCP5	−116.237	34.432	−10.10	−5.34	85.40	81.52	−25.70	−23.22
6050	−116.334	34.266	3.10	1.92	23.90	22.29	5.00	5.28
SCP6	−116.345	34.407	1.70	−2.13	51.00	53.54	6.60	8.35
PAXU	−116.390	34.153	2.80	1.52	12.70	11.42	2.20	3.28
LEDG	−116.439	34.502	−1.30	−2.69	37.10	35.61	0.60	−1.44
MAUM	−116.458	34.419	0.40	−0.19	32.10	26.41	6.70	5.87
7001	−116.469	34.560	−2.00	−2.97	22.80	23.60	−22.20	−18.86
LAZY	−116.514	34.344	0.60	0.87	15.30	15.30	4.30	4.90
MEAN	−116.550	34.405	1.70	0.15	17.90	12.98	1.30	2.36
6056	−116.647	34.370	−0.30	0.19	10.30	6.64	−0.40	0.97
GOL2	−116.889	35.425	−1.00	−0.07	1.90	−0.17	−1.00	−0.58

simply because the source is unique. Unfortunately, we found significant differences when we studied the Hector Mine earthquake using the individual data sets. While this result can be explained by the assumption that there was large afterslip during the first few days after the mainshock, we will present another scenario here, showing that the difference disappears if the main rupture initiation is deeper than the hypocentral depth determined by the regional seismic network, TriNet. After addressing this problem with the inversions constrained by GPS and strong-motion data, we will present our preferred finite-fault model, which is constrained by combining teleseismic body wave, strong-motion, GPS, and surface-break observations.

Hypocentral Depth Sensitivity

We begin with a finite-fault inversion constrained by the GPS data and surface offset. The first model is determined using the GPS data only. Then the surface offset information is added to invert the second fault model; that is, the shallowest elements were allowed to vary roughly 50% from the assigned surface offset values as averaged along each shallow subfault (Fig. 1). The smoothing and minimum moment constraints are used. The W_c is 0.2 in both cases. The two slip distributions are plotted in Figures 4a and 4b, respectively.

Both models explain the GPS observation very well. The χ^2 values are 152 and 157 for the models constrained by GPS only and GPS and surface rupture, in contrast with the initial value of 4256. Comparing the two slip models, it is clear that as the slip on the shallowest subfaults is constrained by the surface break, the slip on the deeper subfaults is amplified. Hence, the surface offset data are a good complement to the sparse GPS measurements. When we have many close fault static observations (e.g., InSar data) (Rosen *et al.*, 2000), however, the surface offset constraint may not be as critical.

The total moment of both models is about 6.2×10^{19} N m, which is slight larger than the seismic moment deter-

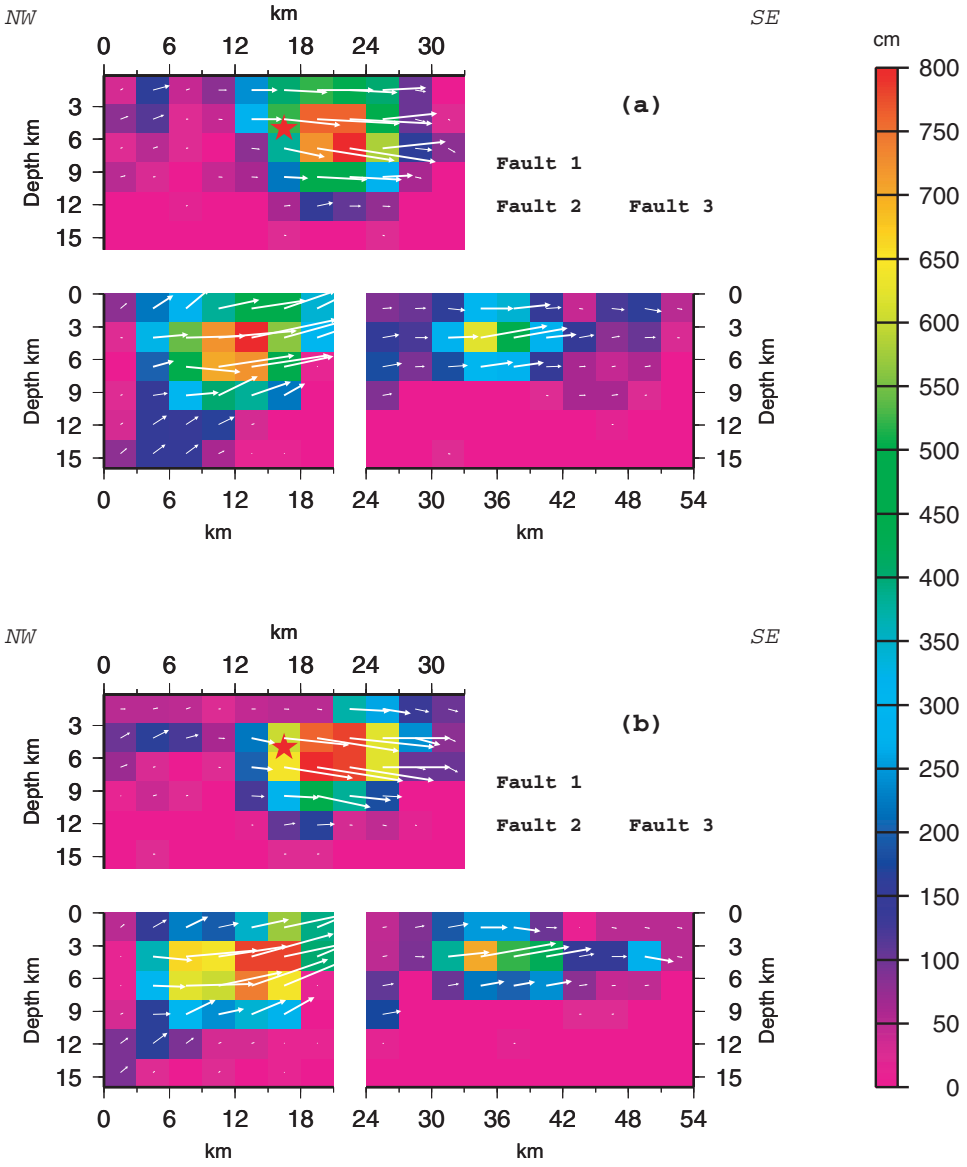

Figure 4. Cross section of the slip distribution determined from modeling the GPS data. Color indicates slip amplitude; arrows show slip direction. The relative positions of three fault segments are indicated in the upper-left corner. (a) Slip distribution constrained by the GPS data only. (b) Slip distribution constrained by GPS plus surface offset measurements.

mined by the Harvard centroid moment tensor (CMT; Table 1). Most of slip occurs on the two branches of the Lavic Lake fault, where the slip amplitudes are up to 7.0 m. Finally, we note that there is significant slip around the hypocenter location determined by the TriNet (red star in Fig. 4) whether we use the surface constraint or not. In addition, this result should not be affected by the initiation position of the main rupture.

The slip distribution determined by the seismic data is no longer independent of the location of the hypocenter. Instead, the slip pattern near the epicenter is strongly affected by the location of the rupture initiation. Unfortunately, such information was not well determined in this case, presumably due to the existence of a foreshock (Dreger and Kaverina, 2000). Even though the strong-motion records at the local stations constrain the epicenter of the main rupture initiation really well, the depth is poorly known, due to the lack of near-source stations (Appendix A). Here, we try to investigate whether we can take advantage of the initiation independence of the static field and obtain a good estimate of the nucleation depth by performing the combined inversions of both strong-motion and GPS data starting at different depths. If the Earth model is correct and there is no afterslip, the model initiating at the correct depth should fit both the strong-motion and GPS data and the surface offset observations simultaneously.

We perform four inversion tests, with individual rupture nucleation depths from 6.7 to 14.8 km. The shallow depth is close to that estimated by TriNet; the latter depth corresponds to maximum depths of seismicity in the ECSZ. Since local strong-motion data clearly show that the signal of the main rupture arrives 2 sec after the first arrival (Appendix A), we delay the rupture starting time a few seconds relative to the hypocentral time (09 h 46 m 41.1 sec, TriNet) to ignore the foreshock. Even though the rupture delay time will change when the main rupture initiation becomes deeper, the variations are small. For example, when the nucleation depths vary from 6.7 to 14.8 km, the rupture delay times change from 2.0 to 1.8 sec.

We weight the strong-motion data 10 times more than that of the GPS data; i.e., $W_{st} = 0.1$ in equation (1). Hence, the models determined are mainly constrained by the strong-motion waveforms. The surface break data are not used in these tests. The inverted slip patterns are summarized in Figure 5, where red stars indicate the positions of the main rupture nucleation.

In general, the slip patterns are very similar. The two large asperities on the faults 1 and 2 and small slip along the Bullion fault appear in all inversions; however, the slip pattern near epicenter does change with the hypocentral depths. The edge of the large asperity on fault 1 is about 6 km away from epicenter in the model with a 6.7-km initiation depth. The area of large slip moves toward the epicenter when the depth of the hypocenter increases. When the hypocenter is greater than 12 km, the slip distribution is visually close to the result of the GPS inversions. The four models also indicate a unique feature: that the slip on the subfaults near the hypocenter is small. This is consistent with the study of Kaverina *et al.* (2000).

Because of the visual similarity, it should be expected that the fit to the GPS data is better when the initiation becomes deeper. The value of χ^2 decreases from 539 to 430 to 337 and 341 as the depth increases from 6.7 to 14.8 km, respectively. Note the sharp variations among models with initiation depths from 6.7 to 12.1 km, and little variation between models with the depths 12.1 and 14.8 km. Similarly, the models with the deeper hypocenter also match the strong-motion data better than the shallower ones; however, the improvements are not very large, the variation in fit for different depths being less than 8%. Such a result is probably due to the fact that most of the strong-motion stations are more than 75 km away from the epicenter. The model with an initiation depth of 12.1 km fits the waveform data best, even though the model with an initiation depth at 14.8 km fits only slightly worse.

We also compare the slip on the shallowest subfaults with the corresponding average surface offsets from Figure 1 (Fig. 5). This indicates that the model with an initiation depth of 14.8 km fits best. In contrast, the model with a 6.7-km initiation depth has a hole around the epicenter where the slip is only about 1 m, compared with average observed surface slip of 4.1 m.

Hence, modeling of the multiple data sets favors the deeper initiation. Since there are not very large differences in fits to both waveform and GPS data between models with a hypocenter at depth of 12.1 or 14.8 km, we choose the deeper one simply because it can explain the surface break better. Similarly, Wald *et al.* (1990) assigned the initiation of the 1987 Superstition Hills earthquake to be 9 km based on waveform modeling, though the hypocentral depth determined by the short-period seismic network was 2 km. Abercrombie and Mori (1994) reported that the location of the large-energy initiation for the Landers earthquake is 4 to 5 km deeper than the network location.

Preferred Finite-Fault Model

We now present an inversion with all four data sets combined. We assume that the beginning of larger slip initiates at a depth of 14.8 km, and choose to initiate the inversion 1.8 sec after the hypocentral time (09 h 46 m 41.1 sec) (see Appendix A). Since the number of data is greatly increased because of combined data set, a main difficulty was to determine the relative weight factors for each dataset and constraints. In this study, we obtain them by trial and error to ensure that none of the data sets are strongly degraded. The values of W_c and W_{st} are 0.1 and 1.0, respectively. The preferred inverted model is shown in Figure 6. Because the effects from a subfault with a small slip are generally small relative to both seismic and static data, the inverted uncertainties in its rise time and rupture velocity are, in turn, usually large. Thus, when we plot our inverted rise times and rupture velocities, only the values of the subfaults with greater than 0.5 m slip are used.

The synthetics generated fit the data quite well. For the GPS data, the χ^2 estimate is 230 (Fig. 3; Table 4). The synthetic seismograms are also consistent with the velocity strong motion and teleseismic *P* and *SH* records (Figs. 7 and 8).

Before the interpretation of the preferred model, we would like to know its limitations. The slip history depends on the velocity structure chosen in our study as indicated by the synthetic test (Ji *et al.*, 2002) and an inversion of the real data (Appendix B). In general, the effects on the slip and rise time distribution are relatively minor, but perturbations to the rupture time contours are not. For the same purpose, we forward predict the InSAR data in Figure 9. InSAR data measures the surface motion in the direction of the radar line of sight during a time interval 1 month before and 4 days after the Hector Mine earthquake (Fialko *et al.*, 2000). Because the radar generally views the ground with very steep angles, the measurements are usually more sensitive to the vertical motion than the horizontal. More accurately, only the horizontal motions in the direction normal to the ground projection of the satellite trajectory have contributions (Rosen *et al.*, 2000). In this case, the satellite moved 194° to the north and looked at the ground with an angle that varied from 17° to 23° to the east. We calculated the ground displacements with the layered Mojave model, and then con-

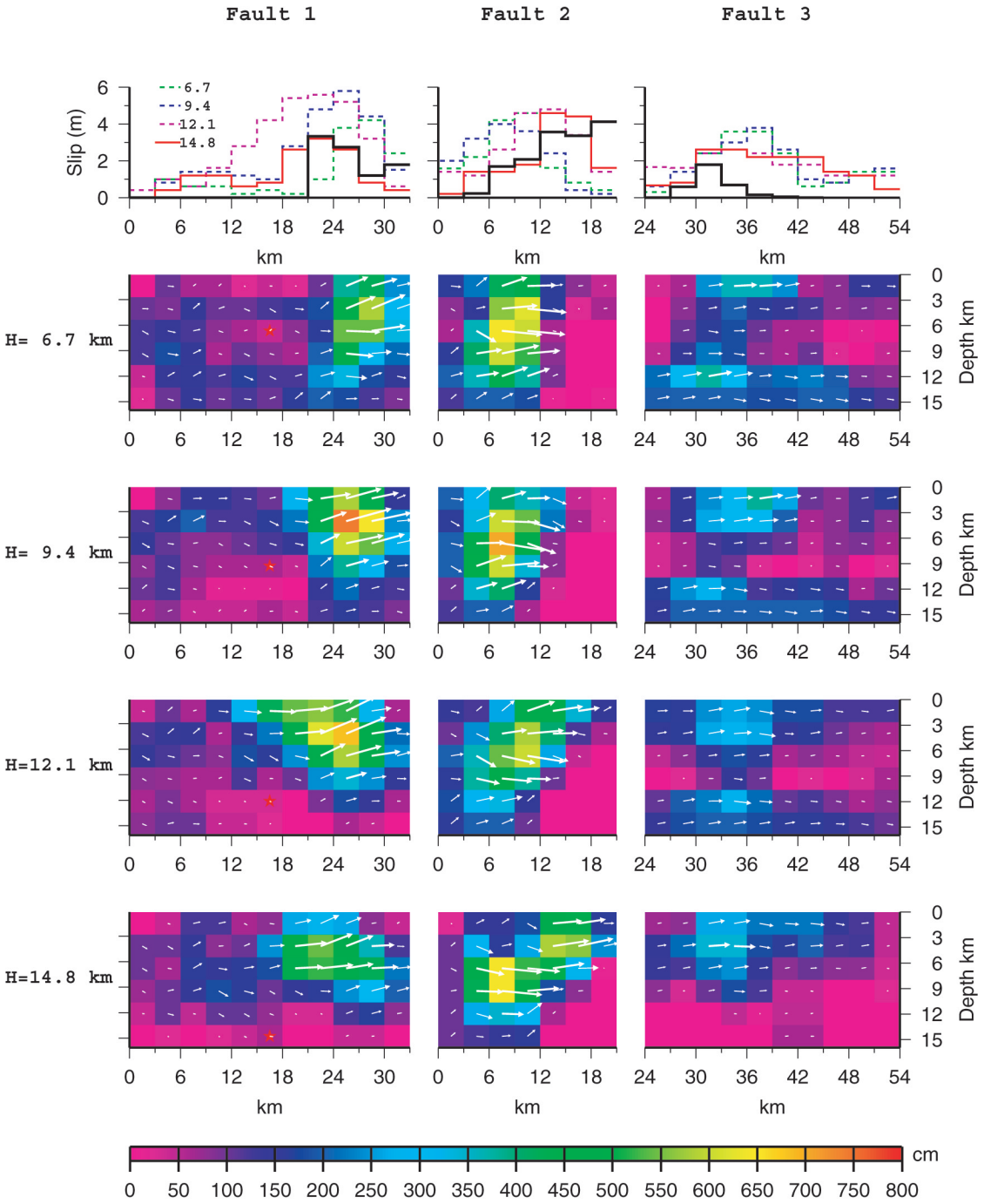

Figure 5. Inversion sensitivity to rupture initiation depth. The four fault slip models have different hypocentral depths and are constrained by strong-motion and GPS data. Red stars indicate the positions of main slip initiations; arrows show slip direction. The color in each pixel displays individual subfault slip amplitude. Predicted surface slips are compared with subfault-averaged observations (black lines, see Fig. 1) in the top diagrams.

verted them to the motions in the radar line of sight. The predicted and observed fields are similar in general (Fig. 9). The apparent discrepancies around the south end of fault 1 are probably caused by the uncertainty in estimating the dip-slip components. Due to the small angle between the extension of fault 1 and the satellite motion direction, the response of the unit dip slip in the radar line of sight is about four times larger than that of the strike-slip motion. The dip-slip motion is generally small in this nearly pure strike-slip event and is hard to determine accurately with our current data sets because of the lack of the close-fault strong-motion stations and because of the large observed error in GPS vertical mea-

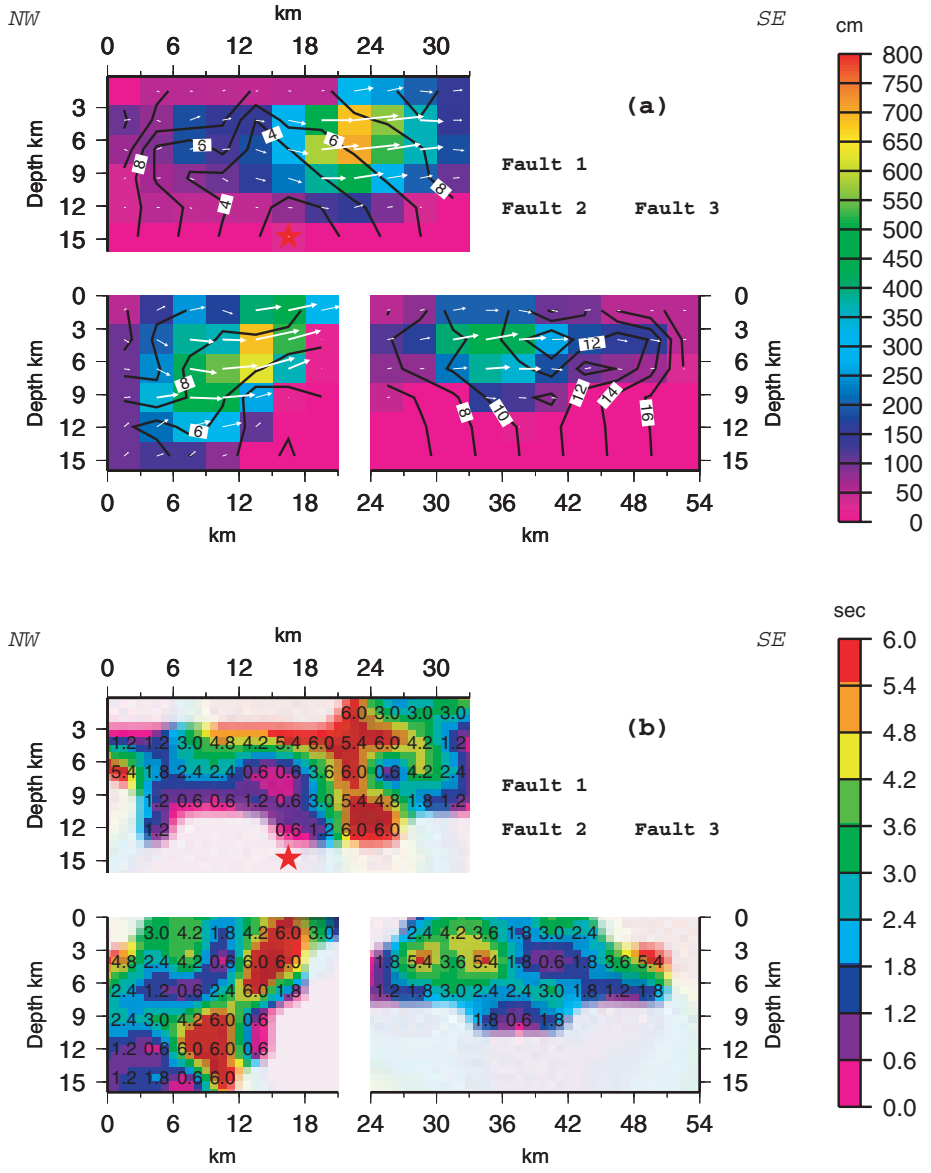

Figure 6. Cross section of the slip distribution determined from inverting combined strong-motion, teleseismic, GPS, and surface rupture data. The Mojave velocity structure is used. Relative positions of three faults are indicated in upper-right corner. A red star indicates the hypocenter. For plotting, we require a 0.5 m minimum slip threshold; i.e., if a subfault has less than 0.5 m slip, the average rupture velocity of the fault segment is used to calculate the initiation time. (a) Slip distribution and rupture initiation time. The slip (cm) is displayed by the color bar. Arrows indicate the rake direction. Contours show the rupture time at 2.0-sec intervals. (b) Rise-time distribution. Numbers on subfaults indicate the subfault rise times. Rise time is not shown for regions where slip is less than 0.5 m.

surements. Hence, further improvement is possible if we include the InSAR data set in our inversion.

Results

We discuss the results of the preferred model in this section. In Table 5, we summarize the averaged values of the slip, rake angle, rupture velocity, and rise time of the whole fault and the individual fault segments. Because the resolution of those values depends on the slip amplitudes, we weight the latter three values by the slip amplitudes. Such values were shown to be insensitive to the inaccurate velocity structure (Ji *et al.*, 2002).

The total moment is 6.28×10^{19} N m. This is slightly larger than other results discussed earlier in Table 1, which likely represents the difference between a point source and a finite-fault approach with multiple fault planes. The 175° average rake angle also agrees well with previous analyses.

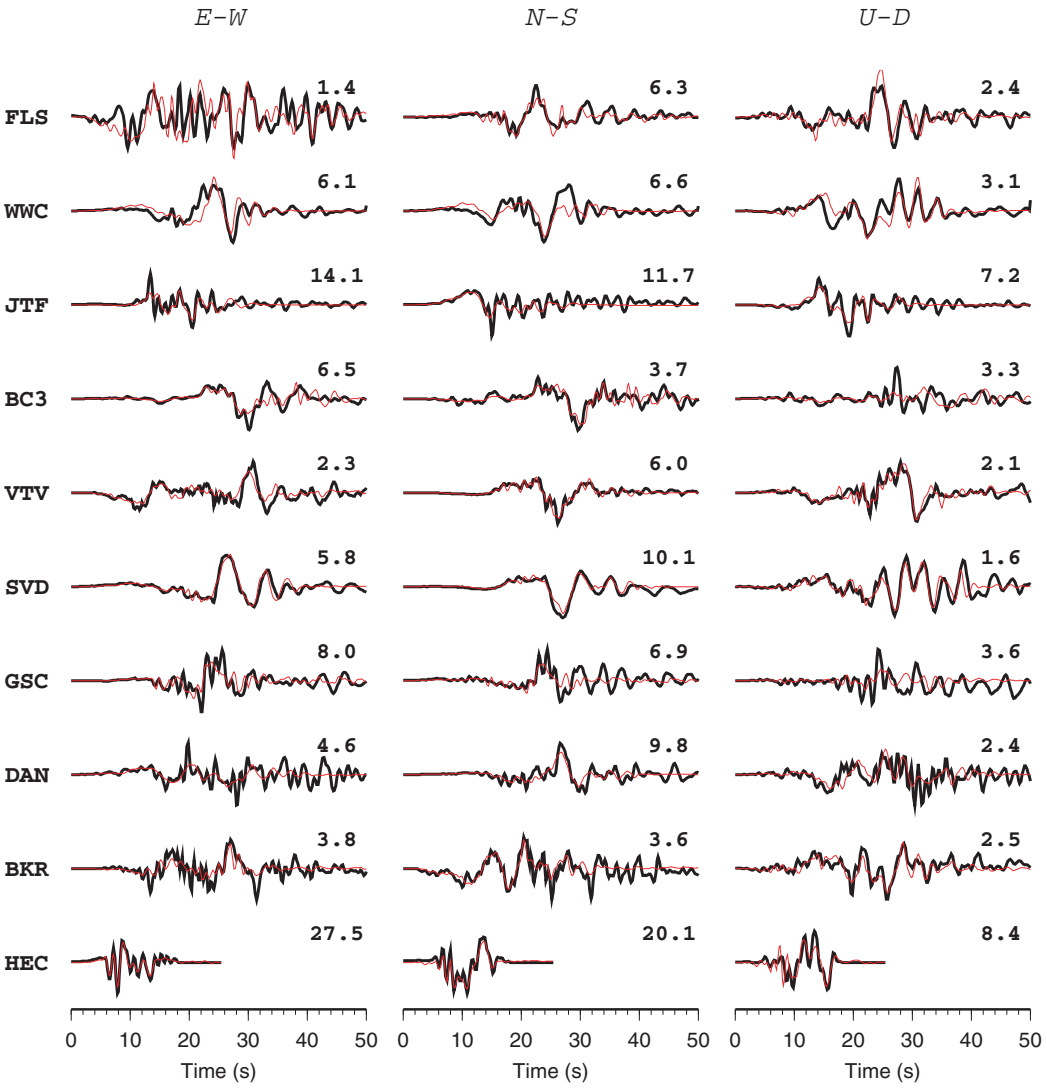

Figure 7. Comparison of the strong-motion observations (thick lines) and synthetic seismograms (thin lines) generated by the preferred model. Station names are indicated at the right. Data are aligned by the *P* arrival time. Peak amplitudes of observed records (cm/sec) are indicated above the end of the traces. The corresponding synthetic seismograms are plotted at the same scale of the observed data.

The average slip amplitude over the entire fault is only about 1.6 m, but 98% of the moment is released on the subfaults with slip amplitudes more than half meter. The average slip on these subfaults increases to 2.6 m. Furthermore, since the three fault segments overlap, after we project the slips of three fault segments into a single plane, the average slip increases to 3.5 m in the top 12 km. The rise times are roughly proportional to the slip amplitudes, and the average slip velocity is about 0.8 m/sec. The average rupture velocity over whole fault is only 1.9 km/sec (or 53% of shear wave velocity), much lower than more typical values of about 75% to 85% of the shear velocity (Heaton, 1990).

The moment releases for fault segments 1, 2, and 3 are 41%, 37% and 22% of the total, respectively. The strike slip component still dominates the slip in three fault segments, but there is a larger thrust component on fault 2 (14%). Both faults 1 and 2 have slower average rupture velocities, about 1.8 km/sec, even though the distributions are not uniform. Their average rise times are about 3.7 sec. On the other hand, fault 3 (Bullion fault) has a relatively faster local rupture velocity (>2.1 km/sec) and a shorter rise time (2.8 sec). These results may imply that the dynamic processes of the Lavic Lake and Bullion faults are different.

Rupture History

The subfault initiation time can be calculated with inverted rupture velocities of individual subfaults. Because the rupture time is resolved only for subfaults with significant slip, when we plot the result, for a subfault with slip less than 0.5 m, we use mean rupture velocity averaged over the

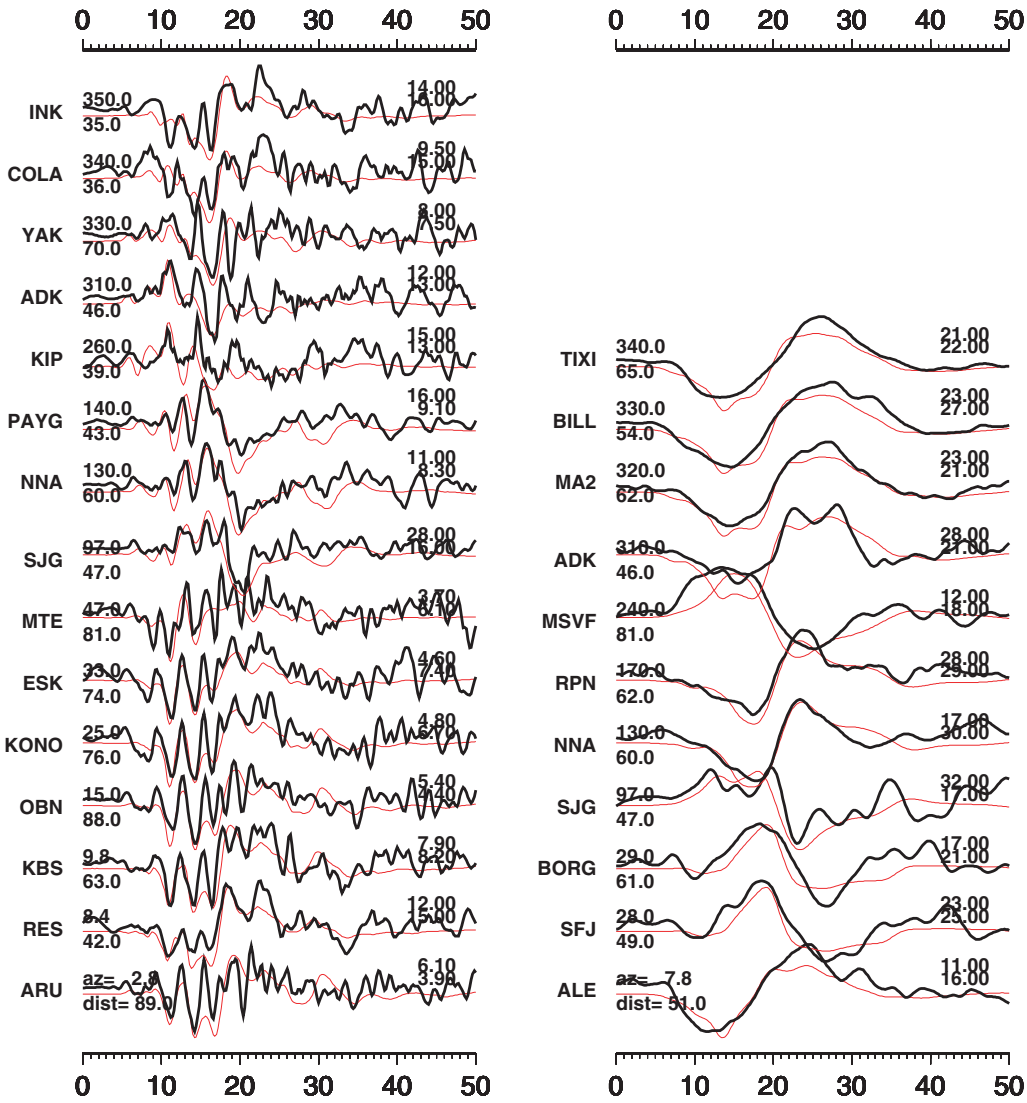

Figure 8. Comparison of the teleseismic velocity records (thick lines) and synthetics (thin lines) generated by the preferred model. The left column shows the comparison of teleseismic *P* waves and the right column shows SH waves. The station names are indicated to the right of traces along with the azimuths and epicentral distances in degrees. The peak amplitudes in mm/sec are indicated above the end of each trace, with the upper number for the data and lower number for the synthetics.

corresponding fault segment (Table 2) instead. The initiation time is depicted by contours with 2.0-sec intervals (Fig. 6).

We give the rupture velocity substantial freedom. The average rupture velocity between hypocenter and rupture region can vary from 1.6 to 3 km/sec. With this approach, the local rupture front speed can be as much as 4.5 km/sec. Furthermore, there is no causal constraint that a subfault further from hypocenter should rupture later then one that is closer. Thus, the local rupture velocity can be negative. However, a subfault with a negative local rupture velocity will be indicated by nonsequential initiation time contours (Ji *et al.*, 2002). In the combined inversion model, the rupture is orderly in the substantial slip regions along fault 1 and 2; however, we find features on fault segment 3 where the surface rupture data imply a complex rupture process, as discussed below.

The main rupture initiated on fault 1, which represents the east branch of the Lavic Lake fault. It then bilaterally propagated in both directions, with different rupture velocities. The slip was small during the first 2 to 3 sec; then the asperity south of the hypocenter started to rupture. Fault 2 was triggered at about the same time and ruptured northward. Significant slip on fault 3 began after about 10 sec. The small slip amplitude along the northern end of fault 3 may not be a reliable feature, because of the lack of close-in data. The total rupture propagated for about 14 sec, and more than 70% of the seismic moment was released by the two large asperities on faults 1 and 2 during the first 10 sec.

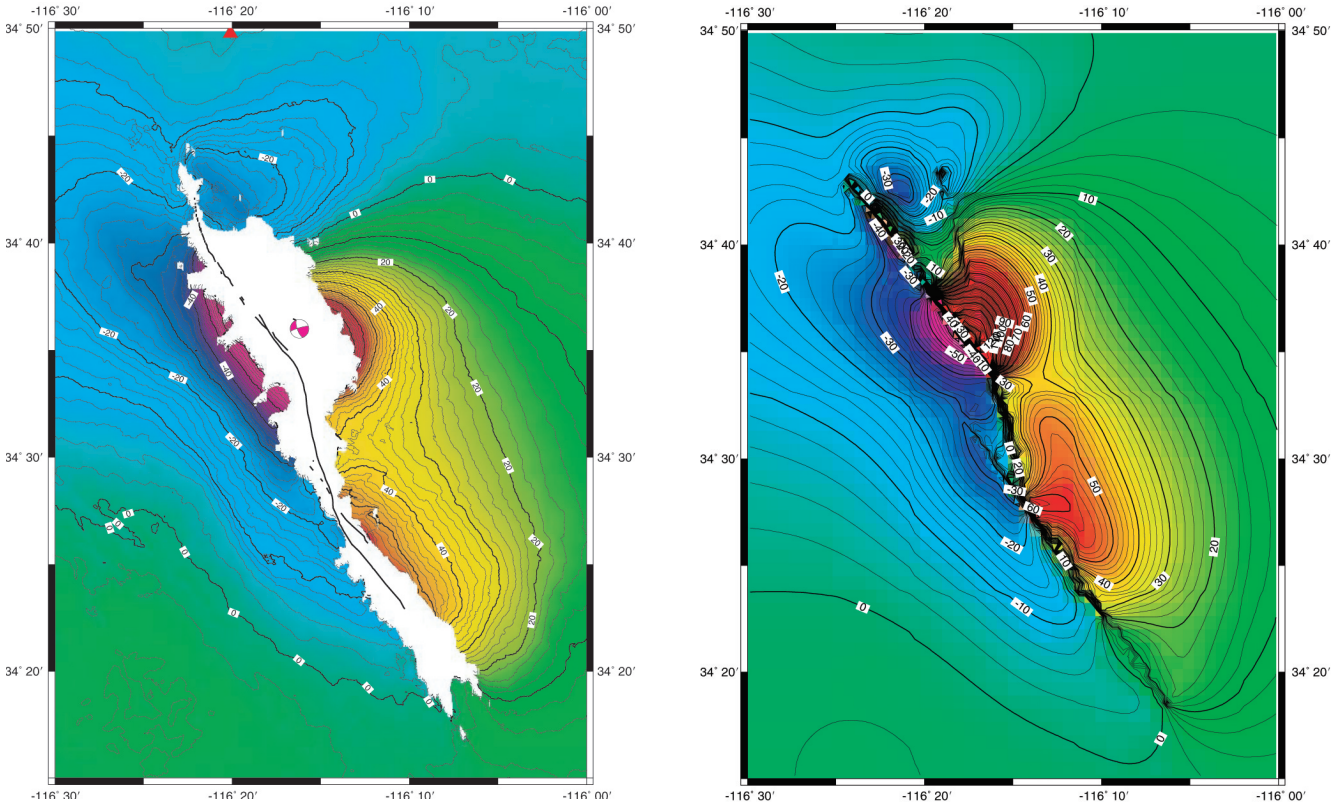

Figure 9. *Left:* Interferometric Synthetic Aperture Radar (InSar) data of the 1999 Hector Mine Earthquake. The azimuth of satellite track is S14°W. The satellite look angle is 17° to 23° to the west. The contours (cm) indicate the displacement field in the direction of the radar line of sight. The surface rupture is displayed by black lines. The epicenter is indicated by the focal mechanism. In the white region, the spatial variation of the coseismic displacement is too large to be measured accurately. *Right:* The synthetic InSar displacements predicted by the preferred slip model. The Mojave model is used to generate the static field. For simplicity, we approximate the look angle as 20°.

Table 5
Summary Information of the Preferred Model

Parameter	Fault 1	Fault 2	Fault 3	Whole Fault
Moment (10^{19} Nm)	2.55	2.30	1.32	6.28
Dislocation (m)	1.6 (2.6)	2.3 (3.0)	0.9 (2.0)	1.5 (2.6)
Rake Angle (°)	178	172	178	175
Rupture Velocity (km/sec)	1.8	1.8	2.1	1.9
Rise Time (sec)	3.7	3.7	2.8	3.5

The dislocation amplitudes of subfaults are used as weights to calculate the average rake angle, rupture velocity and rise time of whole fault and three fault segments. The numbers in brackets are the average dislocation amplitudes for subfaults having more than 0.5 m slip.

The slip history near the initiation region is probably well resolved by the seismic data. During the Hector Mine mainshock, both slip amplitude and rise time on the initiation region are relatively small (Fig. 6). The rise time is about 1 sec, in contrast with the 3.7-sec average rise time of fault 1. The rupture initiation of asperity on fault 2 is also accompanied by a short rise. These two results are well constrained by the high-frequency observations at station HEC (Fig. 10). A shorter rise time at the beginning of rupture has been reported in the studies of several other larger earthquakes (e.g., Northridge earthquake; Hartzell *et al.*, 1996; Wald *et al.*, 1996). Because of the limitation of the inversion, we cannot remove the possibility that the real derivative rise-time function is actually a sharp triangle function followed by a long but small amplitude tail. Such an observation would reflect the strong high-frequency radiation at the boundary of the asperity, as suggested by the theoretic analysis of the dynamic crack rupture (e.g., Madariaga, 1983).

The rupture history of fault 3 is different from that of the fault 1 and 2. It has the fastest average rupture velocity and shortest rise time among the segments. The resolution test (Appendix B) however, also indicates that inversion results in this region are strongly sensitive to the velocity structure. Furthermore, the mapped surface break bifurcates into two distinct branches about 1 km apart at the southern end (Scientists of the USGS *et al.*, 2000; Fig. 1), which implies a more complex fault geometry than the single plane we assumed. This may be the reason that we found some early subfaults (i.e., subfaults rupturing earlier than surrounding

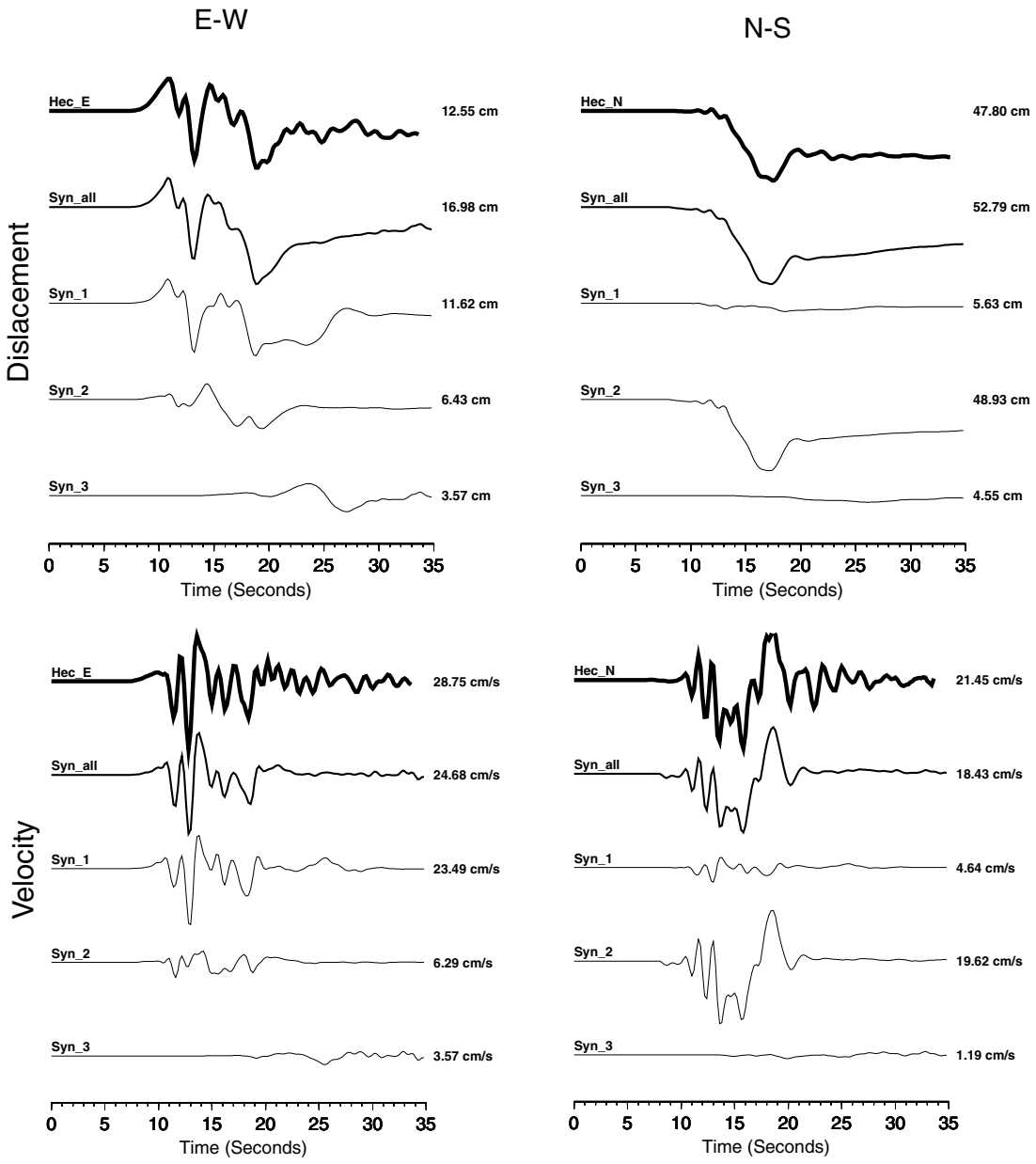

Figure 10. Contributions of the three fault branches at station HEC. We compare horizontal displacement, and velocity records with synthetic seismograms generated from the whole fault (Syn_{all}) and three separate fault branches (Syn_1, Syn_2, and Syn_3). The thick lines show the data.

ones). Unfortunately, no close-in strong-motion station exists that could be used to investigate this in detail.

Y-Structure in the North

An interesting feature of the Hector Mine earthquake model is the peculiar Y-shaped structure in the north. Is it possible to explain the observations using fault 2 alone, without rupture on the northern portion of fault 1? To answer this question, we display the horizontal records of station HEC combined with the synthetic seismograms generated by the three separate fault segments shown in Figure 10.

The horizontal ground motion at the station HEC show very different characteristics in the N–S and E–W directions. The peak amplitude of the ground displacement along the N–S direction (47.8 cm) is three times larger than that along the E–W direction. And the waveform in the N–S direction shows more long-period signal than in the E–W direction. While the radiation pattern can be used to explain the amplitude difference, it is difficult to match the different frequency content using a single source. Because the station HEC is near the nodal plane of fault 1 and N–S is near the radial direction, the large motion must be generated by the

northwestern section (fault 2). This argument has been supported by the inverted slip distribution (Fig. 6). The high-frequency waveform in the E–W direction requires an additional source, however; i.e., if the slip also happens on fault 2, the amplitude on the N–S component will be larger than along the E–W compenent. Figure 6 indicates that the larger velocity motions in the E–W direction are generated by the middle section (fault 1) on which the motion starts early. The rupture time contours on fault 1 can be used to explain the high-frequency character in the E–W direction. During the first 2 to 4 sec of rupture, the rupture front propagates northward with a rupture velocity greater than 2.5 km/sec. Moreover, the subfaults in the rupture region have very short rise times. These combined produce the large peak ground velocity at the E–W component of the station HEC, which is the largest velocity recording during the Hector Mine earthquake. Hence we conclude that the Y-shaped rupture pattern in the north is favored by the observations.

Unfortunately, we cannot find more evidence in the other seismic records. The seismic energy radiated from the subfaults north of the hypocenter is released in the first 10 sec after initiation, which is also the time that two larger asperities on the faults 1 and 2 rupture. Hence, it is difficult to distinguish them uniquely in the more distant strong-motion or teleseismic records.

The occurrence of the Y-structure is not unprecedented in the Mojave events. The surface break of the 1992 Landers earthquake consisted of overlapped multiple faults. Wald and Heaton (1994) found significant slip on the overlapped fault segments in their finite-fault inversion. Without the special source station geometry we have here, however, it is quite difficult to distinguish whether the slip was concentrated on one of fault segments or both (Cotton and Campillo, 1995) or whether they ruptured simultaneously.

Comparison of the Hector Mine and Landers Earthquakes

Since the 1992 Landers and 1999 Hector Mine earthquakes are so close in both space and time, it is natural to compare rupture models from these two events. Both earthquakes occurred in the ECSZ, and are nearly pure strike slip. Moreover, two events involved multiple fault planes, and slip started on the fault segments with a N15°W orientation, which may be explained with the block rotation and faulting model (Nur *et al.*, 1993) or crustal heterogeneity (V. Langenheim, personal comm., 2001).

The average rise time of the Hector Mine earthquake is also close to that of the Landers events. We calculate the weight average rise time of the Landers earthquake based on the slip model of Wald and Heaton (1994). In that study, they used six 1-sec-wide triangles to represent the derivative of the rise-time function on each subfault. We define the rise time as the time required to accumulate from 10% to 90% of the total slip; the average rise times of their fault segments and the entire fault range from 3.8 to 4.3 sec. This result is similar to the 3.6-sec average rise time we find for the Hector Mine earthquake.

The rupture propagation styles and speeds are notably different, however. The Landers earthquake ruptured unilaterally northward, whereas the Hector Mine event ruptured bilaterally. Furthermore, there are significant differences in rupture velocities. Even though about 1 km/sec rupture velocity was reported in the overlapped parts of fault segments (Wald and Heaton, 1994), the average rupture velocity over the entire Landers fault is 2.5 to 2.9 km/sec (Wald and Heaton, 1994; Cohee and Beroza, 1994; Dreger, 1994), or 70% to 80% of average shear wave velocity. This is similar to the average value obtained from other earthquakes (Heaton, 1990). In contrast, the rupture velocity for the Hector Mine events is lower, averaging 1.9 km/sec. Dynamically, a slower rupture velocity implies that more energy is used to fracture rock (Kanamori and Heaton, 2000). This may be explained by either a long slip-weakening distance or a high strength excess, based on the slip weak hypothesis (Guatteri and Spudich, 2000), both of which suggest that the Lavic Lake fault should be stronger than the major faults involving in the Landers earthquake.

Conclusion

We have developed a model of the rupture history of the 1999 Hector Mine earthquake by the combined inversion of strong-motion, teleseismic, and GPS data. The slip amplitude, rake angle, rise time, and rupture velocity are recovered simultaneously. The wavelet transform approach allows time-frequency localization, which allows for recovery of rupture timing and slip distribution. Our model has an average rupture velocity of 1.9 km/sec, but the rupture velocity on the Bullion fault exceeds 2.1 km/sec.

Similar to other large earthquakes (Ellsworth and Beroza, 1995), the Hector Mine earthquake started with a foreshock or nucleation phase of 1.8 sec; the main rupture then initiated deeper (12–15 km). The total slip duration (with the delayed origin time) was about 18 sec, close to the 22- to 24-sec duration of the 1992 Landers event. The total seismic moment was 6.28×10^{19} N m. The rupture on fault 1 (eastern and central branches of the Lavic Lake fault) lasted 10 sec, and contributed greater than 41% of the seismic moment. Most energy is radiated by the asperity south of the hypocenter that had a long rise time. Rupture extended from the surface to over 12 km. Fault 2 (western branch of the Lavic Lake fault) was not triggered until about 3 sec later. It then ruptured for 7 sec, releasing 37% of the total seismic moment. Fault 3 (the Bullion fault) ruptured from 8 to 14 sec, and contributed the remaining 22% of the seismic moment. The slip on this segment was concentrated in the upper 9 km.

In the northern part of the fault system, we find evidence for a Y-shaped rupture pattern, where the two branches ruptured nearly simultaneously.

Acknowledgments

We benefited from discussions with H. Kanamori. We thank M. Simons for providing the InSar figure, E. Hauksson for the aftershock catalog, and D. Agnew for the GPS data. The manuscript benefited significantly from the thoughtful comments by the reviewers S. H. Hartzell, G. C. Beroza, and associate editor V. Langenheim. This project was supported by SCEC Contract Number. NSF EAR-8920136 and by the U.S. Geological Survey under Contract Number 1HQGR0098. The figures were made using GMT (Generic Mapping Tools) software (Wessel and Smith, 1991). This is Contribution Number 8750, Division of Geological and Planetary Sciences, California Institute of Technology.

References

Abercrombie, R., and J. Mori (1994). Local observations of the onset of a large earthquake: 28 June 1992 Landers, California, *Bull. Seism. Soc. Am.* **84,** 725–734.

Agnew, D. C., S. Owen, Z.-K. Shen, G. Anderson, J. Svarc, H. Johnson, K. E. Austin, and R. Reilinger (2002). Coseismic displacements from the Hector Mine, California, earthquake: results from survey-mode GPS measurements. *Bull. Seism. Soc. Am.* **92,** 1355–1364 (this issue).

Aki, K., and P. G. Richards (1980). *Quantitative Seismology: Theory and Methods*, W. H. Freeman and Co, New York.

Cohee, B. P., and G. C. Beroza (1994). Slip distribution of the 1992 Landers earthquake and its implications for earthquake source mechanics, *Bull. Seism. Soc. Am.* **84,** 692–712.

Cotton, F., and M. Campillo (1995). Frequency domain inversion of strong motions: application to the 1992 Landers earthquake, *J. Geophys. Res.* **100**(B3), 3961–3975.

Dreger, D. S. (1994). Investigation of the rupture process of the 28 June 1992 Landers earthquake utilizing terrascope, *Bull. Seism. Soc. Am.* **84,** 713–724.

Dreger, D. S., and D. V. Helmberger (1993). Determination of source parameters at regional distances with three-component sparse network data, *J. Geophys. Res.* **98,** 8107–8125.

Dreger, D. S., and A. Kaverina (2000). Seismic remote sensing for the earthquake source process and near-source strong shaking: A case study of the October 16, 1999 Hector Mine earthquake, *Geophys. Res. Lett.* **27,** 1941–1944.

Ellsworth, W. L., and G. C. Beroza (1995). Seismic evidence for an earthquake nucleation phase, *Science* **268,** 851–855.

Fialko, Y., M. Simons, and D. Agnew (2001). The complete (3-D) surface displacement field in the epicentral area of the 1999 *M*(w)7.1 Hector Mine earthquake, California, from space geodetic observations, *Geophys. Res. Lett.* **28,** 3063–3066.

Graves, R. W., and D. J. Wald (2001). Resolution analysis of finite fault source inversion using 1D and 3D Green's functions. I: Strong motion, *J. Geophys. Res.* **106,** 8745–8766.

Guatteri, M., and P. Spudich (2000). What can strong-motion data tell us about slip-weakening fault-friction law? *Bull. Seism. Soc. Am.* **90,** 98–116.

Hartzell, S. H., and T. H. Heaton (1983). Inversion of strong ground motion and teleseismic waveform data for the fault rupture history of the 1979 Imperial Valley, California earthquake, *Bull. Seism. Soc Am.* **73,** 1553–1583.

Hartzell, S. H., P. Liu, and C. Mendoza (1996). The 1994 Northridge, California, earthquake: investigation of rupture velocity, rise time, and high-frequency radiation, *J. Geophys. Res.* **101**(B9), 20,091–20,108.

Hauksson, E. (2000) Crustal structure and seismicity distribution adjacent to the Pacific and North America plate boundary in southern California, *J. Geophys. Res.* **105,** 13,875–13,903.

Hauksson, E., L. M. Jones and K. Hutton (2002). The 1999 M_w 7.1 Hector Mine, California Earthquake Sequence: Complex conjugate strike-slip faulting, *Bull. Seism. Soc Am.* **92,** 1154–1170 (this issue).

Heaton, T. H. (1990). Evidence for and implications of self-healing pulses of slip in earthquake rupture, *Phys. Earth Planet. Inter.* **64,** 1–20.

Ji, C., D. J. Wald, and D. V. Helmberger (2002) Source description of the 1999 Hector Mine, California earthquake. I. Wavelet domain inversion theory and resolution analysis, *Bull. Seism. Soc. Am.* **92,** 1192–1207 (this issue).

Jones, L. E., and D. V. Helmberger (1998). Earthquake source parameters and fault kinematics in the eastern California shear zone, *Bull. Seism. Soc. Am.* **88,** no. 8, 1337–1352.

Kanamori, H., and T. H. Heaton (2000). Microscopic and macroscopic physics of earthquake, in *GeoComplexity and the Physics of Earthquakes*, J. B. Rundle, D. L. Turcotte, and W. Klein (Editors), American Geophysical Monograph 120, 147–163.

Kanamori, H., H. K. Thio, D. Dreger, E. Hauksson, and T. Heaton (1992). Initial investigation of the Landers, California, earthquake of 28 June 1992 using TERRAscope, *Geophys. Res. Lett.* **19,** 2267–2270.

Kaverina, A., D. Dreger, and E. Price (2000). Source process of the October 16, 1999 Hector Mine Earthquake (M_w 7.2) from the inversion of broadband regional data, submitted to JGR.

Kennett, B. L., and E. R. Engdahl (1991). Traveltimes for global earthquake location and phase identification, *Geophys. J. Int.* **105,** 429–465.

Madariaga, R. (1983). High-frequency radiation from dynamic earthquake fault models, *Ann. Geophys.* **1,** 17–23.

Mori, J., H. Kanamori, J. Davis, E. Hauksson, R. Clayton, T. Heaton, L. Jones, and A. Shakal (1999). Major improvements in progress for southern California earthquake monitoring, *Trans. Am. Geophys. Union* **79,** 217–221.

Nur, A., H. Ron, and G. C. Beroza (1993). The nature of the Landers–Mojave earthquake line, *Science* **261,** 201–203.

Rosen, P. A., S. Hensley, I. R. Joughin, F. K. Li, S. N. Madsen, E. Rodriguez, and R. M. Goldstein (2000). Synthetic aperture radar interferometry—invited paper, Proceedings of the IEEE, **88**(3), 333–382.

Scientists of the U.S. Geological Survey, Southern California Earthquake Center, and California Division of Mines and Geology (2000). Preliminary report on the 10/16/1999 *M* 7.1 Hector Mine, California earthquake, *Seism. Res. Lett.* **71,** 11–23.

Sen, M. K., and P. L. Stoffa (1991). Nonlinear one-dimensional seismic waveform inversion using simulated annealing, *Geophysics* **56**(10), 1624–1638.

Sieh, K., L. Jones, E. Hauksson, K. Hudnut, D. Eberhart-Phillips, T. Heaton, S. Hough, K. Hutton, H. Kanamori, A. Lijie, S. Lindvall, S. F. McGill, J. Mori, C. Rubin, J. A. Spotila, J. Stock, H. K. Thio, J. Treiman, B. Wernicke, and J. Zachariasien (1993). Near-field investigations of the Landers earthquake sequence, April to July, 1992, *Science* **260,** 171–176.

Wald, D. J., and R. W. Graves (2001). Resolution analysis of finite fault source inversion using 1D and 3D Green's functions. II. Combining seismic and geodetic data, *J. Geophys. Res.* **106,** 8767–8788.

Wald, D. J., and T. H. Heaton (1994). Spatial and temporal distribution of slip for the 1992 Landers, California, earthquake, *Bull. Seism. Soc. Am.* **84,** 668–691.

Wald, D. J., T. H. Heaton, and K. W. Hudnut (1996). A dislocation model of the 1994 Northridge, California earthquake determined from strong-motion, GPS, and leveling-line data, *Bull. Seism. Soc. Am.* **86,** S49–S70.

Wald, D. J., D. V. Helmberger, and S. H. Hartzell (1990). Rupture process of the 1987 Superstition Hills earthquake from the inversion of strong-motion data, *Bull. Seism. Soc. Am.* **80,** no. 5, 1079–1098.

Wessel, P., and W. H. F. Smith (1991). Free software helps map and display data, *Eos Trans. Am. Geophys. Union* **72,** 445–446.

Zhu, L., and D. V. Helmberger (1996). Advancement in source estimation techniques using broadband regional seismograms, *Bull. Seism. Soc. Am.* **86,** 1634–1641.

Appendix A

Ellsworth and Beroza (1995) summarized seismic evidence to indicate that beginning of the major slip during earthquakes is usually after a foreshock or a nucleation phase. The records of the Hector Mine earthquake also displayed such a phenomenon. Figure A1 shows the vertical component of the velocity records at several of the closest stations to the earthquake. Note that in the first two seconds, there were very small amplitudes; then, the larger signals arrived at nearly same time. In view of the fact that the relative time-shifts of such larger signals in different stations were within 0.2 sec, the initiation of mainshock was within 2 km of the epicenter determined by TriNet. Because all of those data are more than 75 km away, however, we do not have a very good constraint on the hypocentral depth.

The records of the closest station, HEC, set an upper limit to the nucleation time (Fig. A2). Because the station is close to the *P*-wave nodal plane, we analyze the SH wave on the E–W component. Based on the Mojave model, the Sg wave should arrive at 8.3 sec (T2 in Fig. 12), or 2.4 sec before the observed Sg phase (T3 in Fig. 12). Hence, the nucleation time must be less than 2.4 sec. The difference in nucleation time estimated from Pg and Sg may be caused by inaccurate velocity structure, or deeper or southward initiation of the main rupture. If we use the network epicenter and Mojave velocity structure, however, the depth of the rupture initiation should be around 14 km. In this work, if we assume that the hypocentral depth is 12 to 15 km, then the main rupture starts 1.8 sec later, taking into account the 0.2-s delay caused by a deeper hypocenter.

Appendix B

Sensitivity to the Crustal Velocity Structure

It was pointed out that the velocity structure around the Hector Mine earthquake is relatively simple (Hauksson, 2000). For the inversions presented, we choose the 1D Mojave model to build the Green's functions. This model is not perfect, however, and potential variations should exist compared to the real 3D earth. Such differences, in turn, should

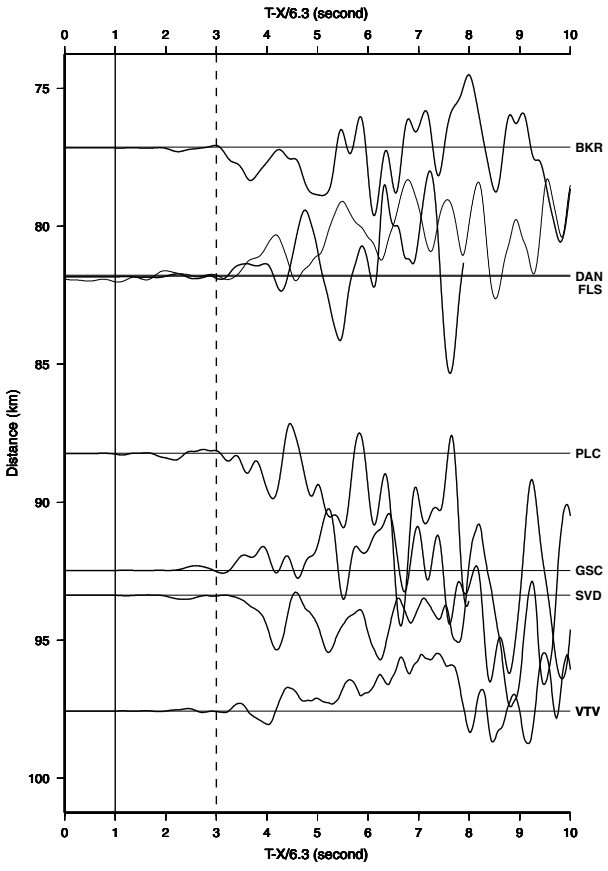

Figure A1. Beginning portion of vertical component velocity records at several nearby stations for the Hector Mine mainshock. The data is low-pass filtered to 2 Hz. The traces were first reduced by a velocity of 6.3 km/sec and then aligned to 1.0 sec. There is little energy in the first two seconds, followed by significant arrivals at all stations.

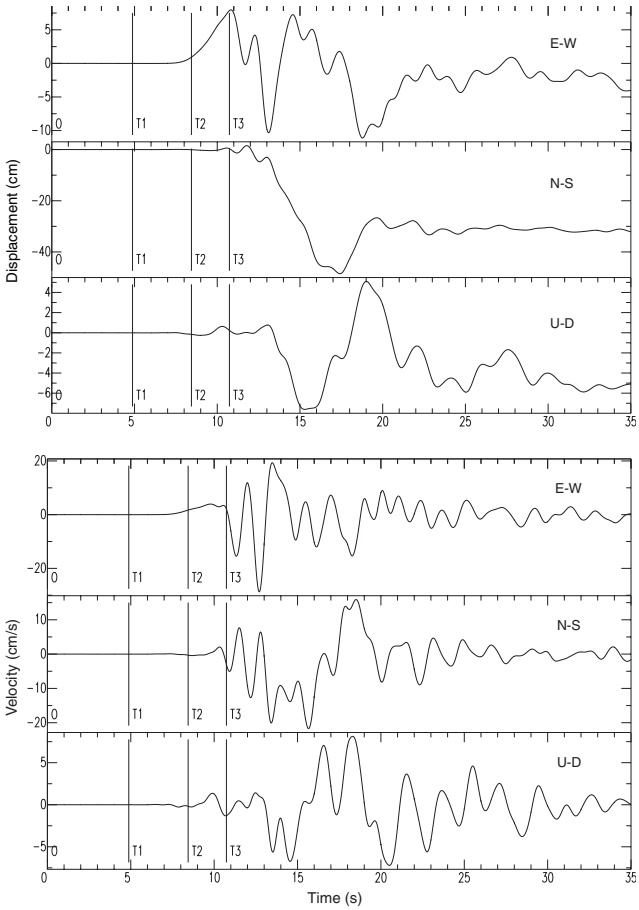

Figure A2. The three-component displacement and velocity records in station HEC. The data are low-pass filtered to 1 Hz. The time-mark T1 indicates the arrival time of P wave. Labels T2 and T3 are the predicted and observed Sg wave arrival times, respectively.

cause the uncertainty in the inverted finite-fault model (Ji *et al.*, 2002). Here, we try to investigate this possible uncertainty by performing an inversion with a different velocity structure.

In our part I (Ji *et al.*, 2002), we discuss the effect of inaccurate velocity structure with synthetic data. This showed that the inverted slip history changes can be significantly affected. Here, we use the southern California standard model (SoCal; see Fig 2; Dreger and Helmberger, 1993) to calculate the Green's functions and invert the fault model with exactly the same parameterization and data sets as those of our preferred model. Note that, in contrast to the resolution test that we used in part I, surface offset data are used here. The result is shown in Figure B1.

In general, the variation in velocity model does not greatly reduce the fit to the data, but the inverted slip history is altered. The inversion to the slip distribution seems to be relatively robust. The overall patterns on fault 1 and 2 are quite similar to the preferred model, but the variation on fault 3 is large. The slip becomes deeper on fault 1, but shallower on fault 2. The largest effect of velocity structures is shown in the inverted rupture time distribution, particularly on fault 3. Even for fault 2, which is close to station HEC, we notice that the contours no longer vary smoothly, as in our preferred

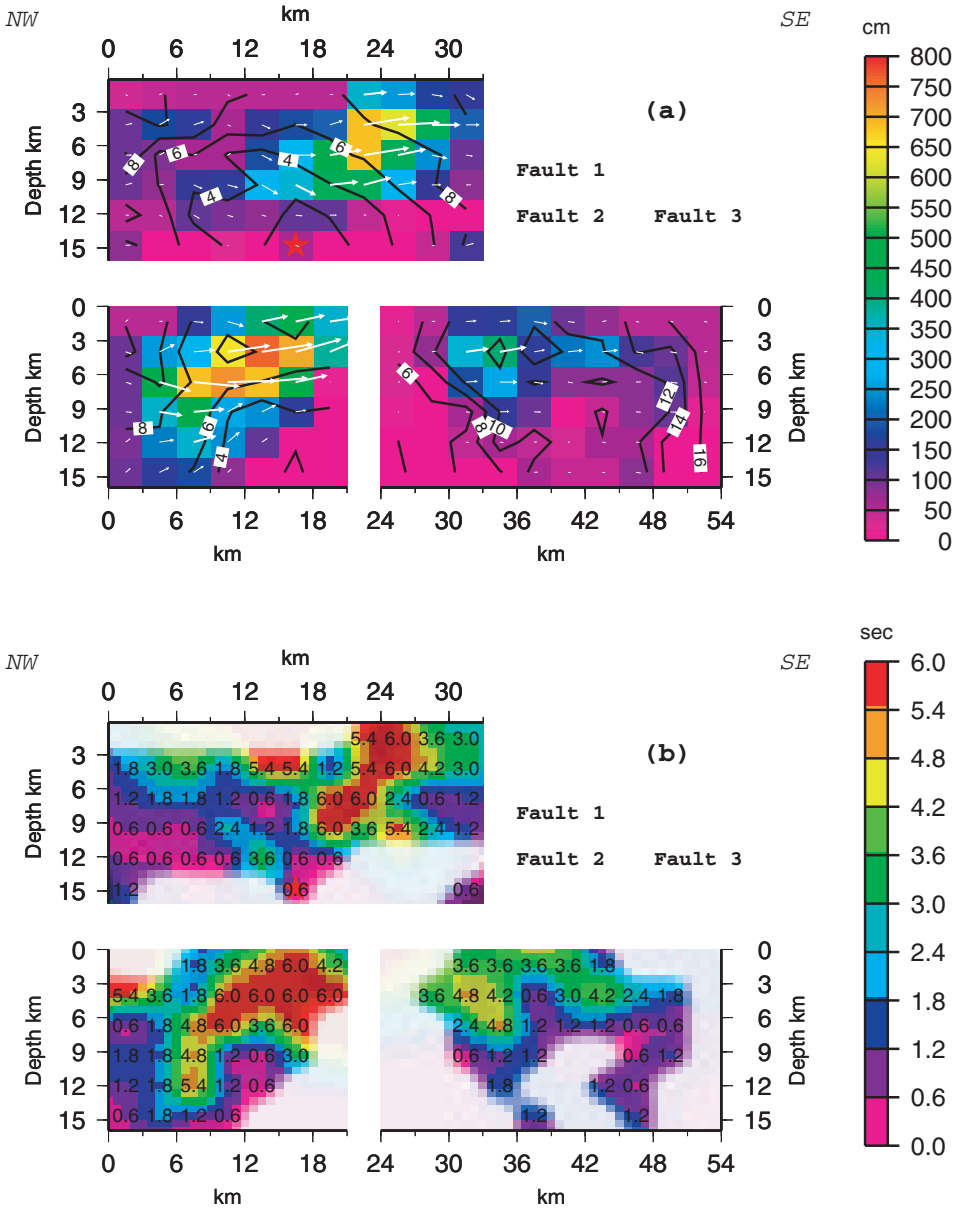

Figure B1. Cross section of the slip and rise-time distributions determined from inverting combined strong-motion, teleseismic waveform, GPS, and mapped surface rupture data. Details as for Figure 6. Note that in this inversion, the Green's functions are generated from the SoCal velocity model (Fig. 2).

model: one subfault slips earlier than the surrounding subfaults. Such phenomena were also observed by the numerical tests in part I. It is relatively difficult to evaluate the effect on the rise-time distribution, simply because small changes in slip distribution bring about large variations in spatial distribution of the rise time. For instance, on fault 2, both models have a long rise-time region (red region in Fig. 6 and Fig. 13), but this region in Fig. 13 extends further southward, accompanying a similar shift in the slip distribution. Hence, for rise-time distribution, the relative pattern is more reliable than the absolute shape, which seems to be preserved.

These results reflect the fact that fault parameters have different sensitivities to the velocity structure. First, in the numerical resolution test performed in part I, we found that the slip distribution is robust except on the near surface subfaults. However, the additional surface constraint resolves this problem here. Second, if the rupture velocity does not change rapidly, the rise time of a subfault usually determines the frequency contents of radiating seismic waves. Unless shallower layers have much lower velocities, the frequency content of the dominant phase, Sg, is very robust with respect to velocity structures. Thus the rise-time distribution is fairly stable. Finally, the variation in velocity structure does affect when the phases reach the strong-motion stations, so rupture velocities must change to compensate such effects. Even though the effect caused by the uncertainty of the Mojave model may be smaller than what we see here, the influence should definitely exist. Hence, when we analyze the results of our preferred model, these possible variations should be taken into account.

Seismological Laboratory
California Institute of Technology
Mail Code 252-21
1200 E. California Blvd.
Pasadena, California 91125
(C.J., D.V.H.)

U.S. Geological Survey
525 S. Wilson Ave.
Pasadena, California 91106
(D.J.W.)

Manuscript received 6 November 2000.